Field Verification of a Computational Fluid Dynamics Model for Wave Transformation and Breaking in the Surf Zone

Sreenivasa C. Chopakatla[1]; Thomas C. Lippmann[2]; and John E. Richardson[3]

Abstract: The commercial computational fluid dynamics model FLOW-3D (Flow Science, Inc., Santa Fe, N.M.) is used to simulate two-dimensional wave transformation and breaking across a naturally barred beach profile. Fine scale pressures and velocities are computed for a 35.5 min period over a two-dimensional beach profile measured during the 1990 Delilah field experiment. The model is driven by observed wave spectra obtained in 8 m water depth, and results compared with a cross-shore array of pressure sensors and current meters extending from near the shoreline to beyond the surf zone and the spatial distribution of wave breaking patterns obtained from video data. In the calculations, wave breaking is a natural consequence of the fluid dynamics and does not require the use of empirical formulations or breaking criteria. Good agreement between modeled and observed wave height transformation, mean cross-shore flow, and wave breaking variability suggests that the model can be used as a numerical laboratory to study the wave breaking and dissipation process in detail, and perhaps lead to improved parametrizations for more computationally efficient numerical models.

DOI: 10.1061/(ASCE)0733-950X(2008)134:2(71)

CE Database subject headings: Breaking waves; Coastal processes; Computational fluid dynamics technique; Fluid dynamics; Nearshore; Surf zone; Surface waves; Turbulence.

Introduction

Breaking of ocean surface gravity waves is a highly nonlinear phenomenon that requires gross simplifications to describe analytically. Despite this difficulty, it is important to include breaking in surf zone wave models, and various numerical approaches have been pursued. Early statistical models do not model individual waves, but rather assumed wave height distribution in the open ocean were based on an underlying narrow band Gaussian process, and thus described by the Rayleigh distribution. Inside the surf zone, wave breaking alters the wave height distribution and various approaches were used to limit the highest wave or modify the distribution in a way that largely depended on water depth. Improved models considered the energy flux balance as a means to calculate wave heights (Battjes and Jannsen 1978; Thornton and Guza 1983). An example of modeled rms wave height, H_{RMS}, transformation and wave breaking distributions (parametrized by the fraction of the number of breaking waves, Q_b) based on a modified Thornton and Guza (1983) model is shown in Fig. 1 (Lippmann et al. 1996a).

One limitation of this type of modeling is that free parameters must be specified and are usually tuned by comparing with field observations. Although the H_{RMS} transformation is well modeled, the breaking distributions specified a priori do not match observations obtained over barred beach profiles (Lippmann et al. 1996b). The model clearly does not reproduce the spatial distribution of the breaking patterns. This is significant because the breaking distributions determine the spatial variation in surface shear stress that drives the circulation. In fact, observations of mean alongshore currents have spatial distribution very similar to the observed Q_b, and cannot be reproduced from the wave height transformation model alone (Church and Thornton 1993; Lippmann et al. 1996b).

The effect of breaking has been modeled by including heuristic dissipation terms in both time (Schaffer et al. 1993) and frequency (Kaihatu and Kirby 1995) domain Boussinesq models. With properly tuned parameters that control the dissipation rate, Boussinesq models predict accurately the wave height decay and shape changes of waves propagating across the surf zone (Chen et al. 1997; Kennedy et al. 2000). Additionally, computational fluid dynamics (CFD) models that solve the unsteady Navier–Stokes equations are being used to simulate spilling and plunging waves over a sloping bed using various techniques to track free surfaces (e.g., Lin and Liu 1998; Bradford 2000). CFD models solve fundamental fluid dynamic equations combined with a fluid tracking method, and require a turbulence closure scheme to properly account for subgrid scale turbulence production, transport, and dissipation during the wave breaking process. Fluid tracking schemes enable CFD models to keep track of complex free surface interfaces. Wave breaking can be interpreted from resulting fluid properties, such as velocity, turbulence, or free surface structures, without having to specify breaking conditions beforehand.

Lin and Liu (1998) and Bradford (2000) successfully simulated Ting and Kirby (1995, 1996) laboratory data using a similar

[1]Pacific Northwest National Laboratory, 1100 Dexter Ave. N., Suite 400, Seattle, WA 98109. E-mail: srinic@pnl.gov

[2]Dept. Civil and Environment Engineering & Geodetic Science, Ohio State Univ., Byrd Polar Research Center, 1090 Carmack Rd., Columbus, OH 43210. E-mail: lippmann.2@osu.edu

[3]President, Blue Hill Hydraulics, Inc., 447 Falls Bridge Rd., Blue Hill, ME 04614.

Note. Discussion open until August 1, 2008. Separate discussions must be submitted for individual papers. To extend the closing date by one month, a written request must be filed with the ASCE Managing Editor. The manuscript for this paper was submitted for review and possible publication on April 18, 2006; approved on December 28, 2006. This paper is part of the ***Journal of Waterway, Port, Coastal, and Ocean Engineering***, Vol. 134, No. 2, March 1, 2008. ©ASCE, ISSN 0733-950X/2008/2-71–80/$25.00.

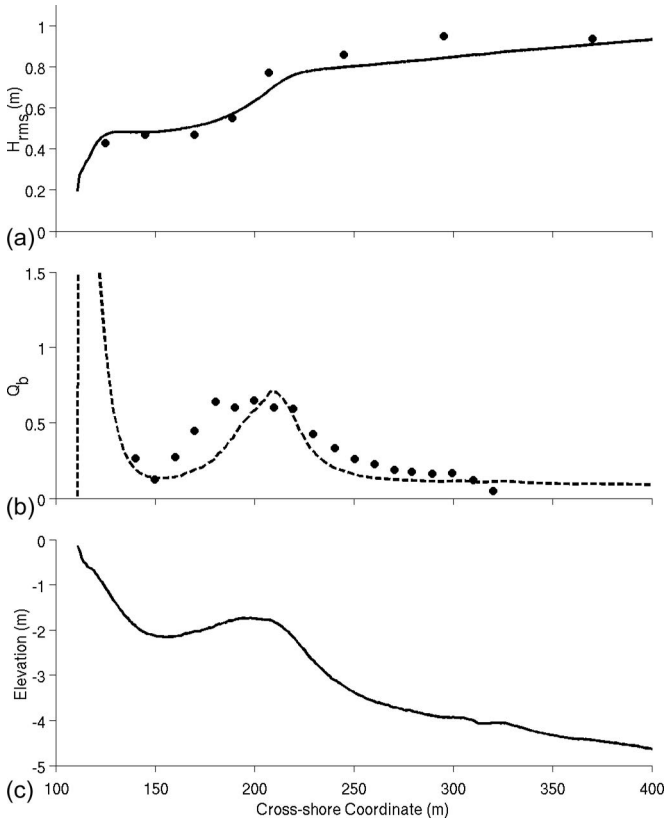

Fig. 1. (a) Ensemble-averaged wave height transformation calculated from Lippmann et al. (1996a), with closed circles indicating wave height data obtained from the 1990 Delilah experiment on October 11, 1990 (Thornton and Kim 1993); (b) percentage of breaking (Q_b) as a function of cross-shore distance, with the field observations as closed circles and the model data as dashed line; (c) beach profile

two-dimensional CFD approach. Ting and Kirby studied spilling and plunging in an experimental tank 40 m long, 0.6 m wide, and 1 m deep with a linear beach profile with 1:35 slope and waves driven by a mechanical paddle prescribed to generate Cnoidal waves. Lin and Liu (1998) compared their CFD model at individual locations with the experimental results and found the model performed well in simulating detailed flow in a single wave breaking event. Bradford (2000) studied instantaneous as well as ensemble-averaged model results, also with good success. Both models simulated 20 s of data citing computational and numerical limitations. The studies strongly support the possibility that CFD models can be used to simulate wave breaking processes at larger scales.

In this work, we examine how well a commercially available CFD model, FLOW-3D (Flow Science, Inc., Santa Fe, N.M.), based on the Reynolds-averaged Navier–Stokes (RANS) equations combined with a turbulence closure model and free surface tracking scheme, can compute cross-shore wave transformation and wave breaking at prototype field scales. In the next section, the governing fluid dynamic equations, turbulence closure schemes, and free surface equation are described. The FLOW-3D model and boundary conditions are described next, followed by a description of the model setup. Model results are compared to field observations of H_{RMS}, Q_b, and mean cross-shore flow obtained during the 1990 Delilah field experiment. The space–time evolution of model results is presented, followed by discussion and conclusions.

Governing Equations

Waves in the present problem are assumed to propagate in a shore normal direction and that fluid dynamics are assumed uniform in the alongshore direction; thus, the problem reduces to a two-dimensional case, where positive onshore represents the cross-shore coordinate and positive upward the vertical coordinate. Two velocity components and pressure are determined from the Reynolds-averaged Navier–Stokes equations

$$\frac{\partial u}{\partial t}+u\frac{\partial u}{\partial x}+w\frac{\partial u}{\partial z}=\frac{-1}{\rho}\frac{\partial p}{\partial x}+\frac{1}{\rho}\left(\frac{\partial \tau_{xx}}{\partial x}+\frac{\partial \tau_{xz}}{\partial z}\right) \tag{1}$$

$$\frac{\partial w}{\partial t}+u\frac{\partial w}{\partial x}+w\frac{\partial w}{\partial z}=\frac{-1}{\rho}\frac{\partial p}{\partial z}-g+\frac{1}{\rho}\left(\frac{\partial \tau_{xz}}{\partial x}+\frac{\partial \tau_{zz}}{\partial z}\right) \tag{2}$$

and the continuity equation for an incompressible fluid given by

$$\frac{\partial u}{\partial x}+\frac{\partial w}{\partial z}=0 \tag{3}$$

where u and w=horizontal and vertical velocities; p=pressure; and t=time.

The average shear stresses are defined as

$$\tau_{xx}=2\rho(\nu+\nu_T)\frac{\partial u}{\partial x},\quad \tau_{xz}=\rho(\nu+\nu_T)\left(\frac{\partial u}{\partial z}+\frac{\partial w}{\partial x}\right)$$

$$\tau_{zz}=2\rho(\nu+\nu_T)\frac{\partial w}{\partial z} \tag{4}$$

where ν=molecular viscosity and ν_T=eddy viscosity. Molecular viscosity is an intrinsic property of the fluid property, whereas the eddy viscosity arises from the turbulence dynamics and is given by the expression $\nu_T=C_\mu k^2/\varepsilon$, where k=turbulence kinetic energy; ε=dissipation rate; and C_μ=empirical constant.

Turbulence transport equations are needed to determine k and ε

$$\frac{\partial k}{\partial t}+\left(u\frac{\partial k}{\partial x}+w\frac{\partial k}{\partial z}\right)=P+D_k-\varepsilon \tag{5}$$

$$\frac{\partial \varepsilon}{\partial t}+\left(u\frac{\partial \varepsilon}{\partial x}+w\frac{\partial \varepsilon}{\partial z}\right)=\frac{C_1\varepsilon}{k}\nu_T P+D_\varepsilon-C_2\frac{\varepsilon^2}{k} \tag{6}$$

where P (a shear production term), D_k, and D_ε are given by

$$P=\frac{1}{\rho}\left(\tau_{xx}\frac{\partial u}{\partial x}+\tau_{xz}\left(\frac{\partial u}{\partial z}+\frac{\partial w}{\partial x}\right)+\tau_{zz}\frac{\partial w}{\partial z}\right) \tag{7}$$

$$D_k=\left(\frac{\partial}{\partial x}\left(\frac{\nu+\nu_T}{\sigma_k}\frac{\partial k}{\partial x}\right)+\frac{\partial}{\partial z}\left(\frac{\nu+\nu_T}{\sigma_k}\frac{\partial k}{\partial z}\right)\right) \tag{8}$$

$$D_\varepsilon=\left(\frac{\partial}{\partial x}\left(\frac{\nu+\nu_T}{\sigma_\varepsilon}\frac{\partial \varepsilon}{\partial x}\right)+\frac{\partial}{\partial z}\left(\frac{\nu+\nu_T}{\sigma_\varepsilon}\frac{\partial \varepsilon}{\partial z}\right)\right) \tag{9}$$

There are five free parameters in Eqs. (5)–(9), C_1, C_2, σ_ε, σ_k, and C_μ. In most turbulence closure schemes, parameter values are obtained from the literature (e.g., Launder and Sharma 1974). For this work we utilize the Renormalized Group (RNG) extension of the $k-\varepsilon$ model introduced by Yakhot et al. (1992) and used by Bradford (2000) and Chopakatla (2003). In the RNG model $C_2=1.68+C_\mu\beta^3(1-0.2283\beta)/(1+0.012\beta^3)$, where $\beta=k/\varepsilon(P/\nu$

$+\nu_T)^{1/2}$. We use literature recommended values for the remaining four turbulence parameters taken from Yakhot et al. (1992): $C_\mu=0.085$, $C_1=1.42$, $\sigma_k=1.39$, and $\sigma_\varepsilon=1.39$.

Fluid Tracking Scheme

There are three issues associated with numerical representation of free surfaces in a rectangular grid system: numerical description of location and shape of the free surface, advection of the free surface in time, and free surface boundary conditions (Hirt and Nichols 1981). Methods have been developed to address the first issue such as height functions and line segment methods; however, these schemes are unable to resolve complicated interfaces (Hirt and Nichols 1981). The marker and cell method (Harlow and Welch 1965) is a successful approach to describe free surfaces; however, this scheme requires large storage and computational effort and is thus impractical for wave problems.

To overcome the limitations of the marker and cell method, a volume of fluid (VOF) scheme (Hirt and Nichols 1981) is utilized that associates each grid cell with a parameter (denoted by F), whose value ranges between zero and unity, where it is unity if the cell is completely filled with fluid and zero if empty. F represents the fluid fraction of the cell and therefore cells with a fractional F value must contain a free surface. The shape and location of the free surface is a natural consequence from the method because the spatial derivative of F can be used to calculate direction of boundary normal. F is governed by an advection equation in space and time, given by $\partial F/\partial t+\partial Fu/\partial x+\partial Fw/\partial z=0$. The VOF method has minimum storage requirements because each cell is associated with just one parameter value, and has proven to be highly robust at representing complex fluid interfaces.

Numerical Solution

In this work, we use the commercial CFD software, FLOW-3D, to solve the fluid dynamic equations. FLOW-3D is used widely in varied commercial and engineering applications. FLOW-3D uses a fixed rectangular grid (Eulerian approach), and overcomes the problem of incorporating geometry in a structured grid by using the Fractional Area Volume Obstacle Representation method (FAVOR; Flow Science Inc. 2002). In FAVOR four parameters are recorded for each cell (area fractions of three faces and volume fraction of the cell) and equations are formulated in terms of these parameters to horizontally block portions of each cell within the obstacle.

Each cell in the flow region is associated with local average values of the dependent variables; scalars are represented at the cell center and vectors at the center of cell faces. Finite-difference approximations to the momentum equations (1) and (2), assuming we are at time level n, are discretized as

$$u_{i,j,l}^{n+1}=u_{i,j,l}^{n}+\delta t^{n+1}\left(-\frac{p_{i+1,j,l}^{n+1}-p_{i,j,l}^{n+1}}{(\rho\delta x)_{i+1/2,j,l}^{n}}+T_x\right) \tag{10}$$

$$w_{i,j,l}^{n+1}=w_{i,j,l}^{n}+\delta t^{n+1}\left(-\frac{p_{i,j,l+1}^{n+1}-p_{i,j,l}^{n+1}}{(\rho\delta x)_{i,j,l+1/2}^{n}}+T_z\right) \tag{11}$$

where i,j,l=indices of cell in the mesh for the x,y,z coordinates and T_x and T_z are terms involving the spatial gradients, $(\rho\delta x)_{i+1/2,j,l}=(\rho_{i,j,l}^{n}\delta x_i+\rho_{i+1,j,l}^{n}\delta x_{i+1})/2$. A standard divergence form (donor-cell approximation) for the spatial gradient terms involving advection, such as $u\partial u/\partial x$, tends to be inaccurate for nonuniform meshes; thus a modified donor-cell approximation is employed that is accurate even for a nonuniform mesh (Flow Science Inc. 2002). Discretization for $u\partial u/\partial x$ in this scheme is given as

$$(u_r-\alpha u_r)\frac{(u_{i+1,j,l}-u_{i,j,l})}{\delta x_{i+1}}+(u_s+\alpha u_s)\frac{(u_{i,j,l}-u_{i-1,j,l})}{\delta x_i} \tag{12}$$

where $u_r=(u_{i+1,j,l}+u_{i,j,l})/2$ and $u_s=(u_{i,j,l}+u_{i-1,j,l})/2$. The basic idea is to weigh upstream and downstream values with factors $(1+\alpha)$ and $(1-\alpha)$, respectively. When $\alpha=1$, a standard divergence form is recovered and when $\alpha=0$, Eq. (12) takes the form of a second-order, central difference method. In the present problem a value of $\alpha=0.3$ is used as recommended by Lin and Liu (1998) and Bradford (2000).

The continuity equation (3) is approximated as

$$\frac{u_{i,j,l}^{n+1}-u_{i-1,j,l}^{n+1}}{\delta x_i}+\frac{w_{i,j,l}^{n+1}-w_{i,j,l-1}^{n+1}}{\delta z_l}=0 \tag{13}$$

The velocities computed from the momentum equations will not exactly satisfy the continuity equation. Therefore, the model solves the momentum and continuity equations iteratively using a pressure correction scheme involving coupled momentum and continuity equations. In the first step, velocities at new time level are estimated by evaluating Eqs. (10)–(12) using the pressure available from the previous time level. The pressure correction needed to satisfy Eq. (13) is calculated as $\delta p=-S(\partial S/\partial p)$, where S=left-hand side of Eq. (13). A new pressure value is determined by $p+\delta p$, which is then used in Eqs. (10)–(12) to generate new velocities. Convergence of the iteration is achieved when all cells satisfy Eq. (13) within some tolerance level. Convergence can be accelerated by multiplying δp by some overrelaxation factor Ω ($\Omega=1.4$ in this work).

Boundary Conditions

Waves are input at the left-hand boundary by specifying surface elevation, η, and velocities, u and w, at each grid point along the boundary. These values can be specified either analytically from any suitable wave theory or from field data, as is done herein. Additionally, the still water level and a nonzero, ambient value for k and ε are specified everywhere in the domain. Along the bottom, the vertical velocity is assumed to go to zero (a wall boundary condition with no flow through the bottom) and the no-slip condition applies. At the bottom boundary, we set $k=u_*^2\sqrt{C_\mu}$ and $\varepsilon=\tilde{u}u_*^2 7d$, where u_*=local shear velocity; $\tilde{u}$=component of the velocity parallel to the wall orientation; and d=normal distance of the computed velocity from the wall.

At the free surface, advective and diffusive fluxes of k and ε are set to zero (Bradford 2000). Pressure in the free surface cell is not adjusted by iteration, but set by interpolating (or extrapolating) the desired pressure at the surface and inside any neighboring cells (Hirt and Nichols 1981). Flow properties are assumed to be uniform in the alongshore direction, and lateral boundaries are symmetric. The shoreward boundary can be anything because the beach obstacle blocks the flow. The obstacle takes on the bottom boundary condition.

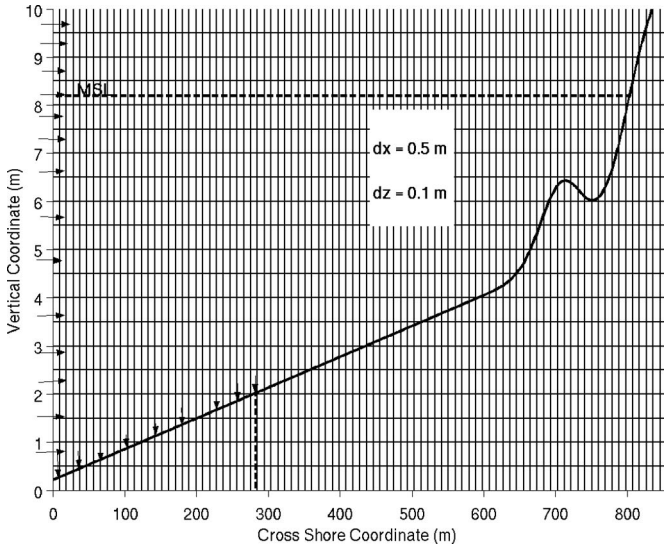

Fig. 2. Schematic of the domain and grid layout for model runs performed with FLOW-3D. The domain is 850 m in the cross-shore direction and 12 m vertically with still water level 8.19 m from the bottom at the seaward boundary. Random waves are generated at the left-hand boundary (from observations) and there is a sink in the deepest one-third of the domain (shown by downward arrows). The computational mesh is uniform with 1,700 cells in the cross-shore direction and 120 cells in the vertical direction (note that the mesh cells shown are purely for schematic purposes).

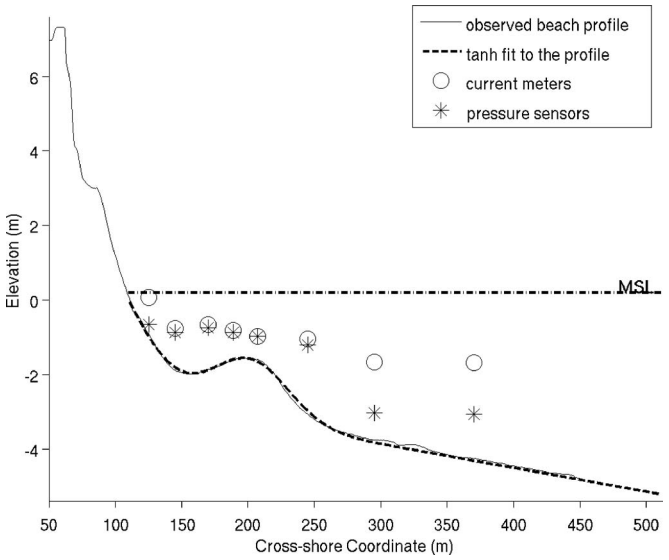

Fig. 3. Beach profile measured in the field on October 11, 1990, during the Delilah experiment. The horizontal axis is cross-shore distance in FRF coordinates, and the vertical axis is elevation relative to NGVD. Analytical fit [Eq. (14)] to the profile is shown by dashed line. Velocity and pressure data were collected at eight locations indicated by circles and asterisks, respectively.

Numerical Methods

Domain Setup

The modeling domain is 850 m horizontally and 12 m vertically with 0.5 m horizontal and 0.1 m vertical cell sizes (Fig. 2). The bathymetry is defined by an analytical approximation of the sand-bar profile observed in the field given by

$$h = x\tan\beta_2 + \frac{a_1}{\tan\beta_1}(\tan\beta_1 - \tan\beta_2)\tanh\left(\frac{x\tan\beta_1}{a_1}\right) - a_2\exp\left(\left[-5\left(\frac{x-x_c}{x_c}\right)^2\right]\right) \quad (14)$$

where $\tan\beta_1$=foreshore slope; $\tan\beta_2$=offshore slope; x_c=location of the bar crest; and the coefficients a_1 and a_2 are determined by fitting the profile to the measured bathymetry (Lippmann et al. 1999). A comparison of the measured profile and that produced by Eq. (14) with $\tan\beta_1=0.0701$, $\tan\beta_2=0.0064$, $a_1=2.93$, $a_2=1.6$, and $x_c=92$ is shown in Fig. 3.

Sink Term

The slow build up of fluid is a common problem encountered in numerical wave problems. In numerical models fluid surfaces are not continuous but approximated using a discretization scheme that over time may lead to excess mass being input in to the domain. In the present model, this problem is alleviated by an artificial sink term along the deepest one-third of the bottom boundary of the domain (Fig. 2), so that it does not interfere with fluid dynamics near the surf zone. An estimate for the sink rate, S_r, was determined experimentally and given by $S_r=(V_f-V_i)\rho/t$, where V_i and V_f=volume of fluid in the domain at the start and end of a test simulation, respectively. The sink rate, 300 kg/s, was found to be so small that it did not have any noticeable effect on the fluid dynamics. In terms of surface height changes, the sink rate corresponds to a decrease in mean water level at a rate of 0.00042 m/s, and thus had negligible impact on the adjacent wall boundary conditions (described earlier). This empirical sink rate approximately balanced the excess fluid put into the domain at the seaward boundary.

Initial and Boundary Conditions

Initial conditions were that the water level is at 8.19 m (based on tidal elevation at the time of data collection), water motion is zero, turbulent kinetic energy throughout the interior of the domain is uniformly assumed to be 2.2×10^{-5} m^2 s^{-2}, and at the inflow boundary $k=2.2\times10^{-3}$ m^2 s^{-2} and $\varepsilon=4.114\times10^{-2}$ m^2 s^{-3} following Bradford (2000).

Random waves are prescribed at the inflow boundary by near-bottom pressure data observed in the field. Conversion from bottom pressure to cross-shore and vertical velocities at each depth is accomplished by linear theory approximations (Guza and 1980). Data at the boundary is input at a frequency of 4 Hz and specified vertically every 0.1 m. Time stepping in FLOW-3D is generally nonuniform and adjusted such that fluid does not cross more than one computational cell over one time step, Δt, and is limited by the Courant condition $\Delta t<\min(\Delta x/u, \Delta z/w)$, where Δx and Δz=horizontal and vertical grid sizes, respectively. Time steps generally do not correspond to the input time series and grid locations do not correspond to input spatial data locations; therefore, input data are linearly interpolated to prescribe the flow at specific times and at all spatial locations at the boundary. Using linear theory and linear interpolations to specify wave forced boundary conditions in 8 m water depths is reasonable [as shown by Guza and (1980)], except, perhaps, near the crests of the waves. Including nonlinear effects near the crests of the waves would slightly modify the boundary conditions impacting the sink

rate used to conserve mass in the domain (discussed earlier), and could result in some change in the fluid response right near the seaward boundary. As our focus is on the larger scale response across the domain, we have ignored this effect (assumed to be small).

Field Methods

The model is driven by observation of the wave spectrum obtained in 8 m water depth from a bottom mounted pressure sensor. The simulated wave transformation, breaking, and mean cross-shore flow will be compared (later) with observations obtained from an array of pressure gauges and current meters spanning the width of surf zone (Fig. 3) and video observations of wave breaking distributions (shown in the middle panel of Fig. 1).

The field data examined in this study were obtained on a sandy, barred ocean beach during the Delilah field experiment, held at the Army Corps of Engineers Field Research Facility in Duck, N.C. in the fall of 1990. For details of the experiment see Birkemeier (1991) and and Kim (1993). During Delilah, there was a single, persistent longshore sandbar in the surf zone approximately 80 m offshore, with a bar trough relief of about 0.5 m over 50 m. The cross-shore profile from October 11 is shown in Fig. 3.

Bidirectional velocity and near-bottom pressure measurements were collected at nine locations along a cross-shore transect that spans the surf zone (Fig. 3). The instruments were sampled at 8 Hz. For comparison to the model, a 35.5 min record beginning at 1000 h EST October 11 was used. Mean wave angle observed in 8 m water depth was approximately 38° CCW from shore normal, with dominant wave period of about 8 s. H_{RMS} (shown in the upper panel of Fig. 1) and mean cross-shore flow (shown later) will be compared to the model.

Wave breaking observations are obtained by counting the number of breaking waves in the video records following the methods described in Lippmann and Holman (1991). The spatial distribution of the fraction of wave breaking, Q_b, is determined by dividing the number of breaking waves by the total number of waves [determined from wave pressure time series; and Guza (1983)]. The spatial distribution of breaking waves observed at approximately 1000 hrs on Oct 11 is shown in Fig. 1.

Results

Model Simulations

The model was run for 35.5 min. Model data were sampled at 5 Hz at prescribed locations within the domain, including those where the current meters and pressure sensors were located (Fig. 4). Inside the surf zone, denser arrays of locations were sampled to better describe the flow. Sea surface elevation time series were used to describe the cross-shore wave transformation and collected every 1 m across the entire domain. Finally, turbulence and dissipation in the top 10 cm of the water column were averaged every 1 m in the cross-shore direction as a means to quantify the spatial and temporal variation in wave breaking patterns.

Snapshots of the model, shaded by TKE and dissipation rate, 1,650 s into the run are shown in Fig. 5. Random waves, entering the domain from the left boundary, propagate to the right of Fig. 5, and evolve nonlinearly in response to changes in water depth. The waves steepen and pitch forward, and eventually break over

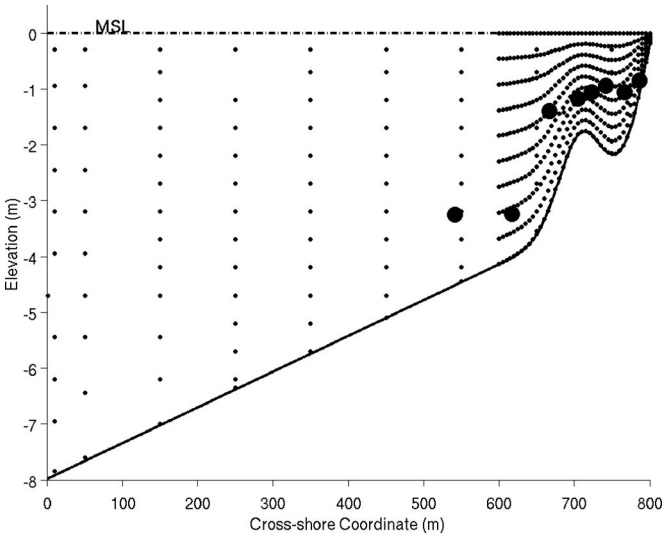

Fig. 4. Grid locations where time series of horizontal and vertical velocities were retained from the FLOW-3D model run. Large closed circles indicate locations of velocity sensors in the Delilah experiment (also shown in Fig. 3). Sensors are densely packed close to the sandbar and in shallow depths to better evaluate velocity changes due to wave breaking.

the sandbar. Some waves continue to actively break across the trough; others reform in the trough and break again at the shoreline where they are allowed to move up and down the beach face generating a swash zone. Wave breaking is identified in the TKE shaded plot by high turbulent intensities primarily confined to a narrow region along the front face of the wave. Turbulence is advected downward in the water column and on–offshore by currents. Average turbulent intensities along the front face of the wave right near the surface are used to identify breaking waves. Breaking distributions are then compared to field data where

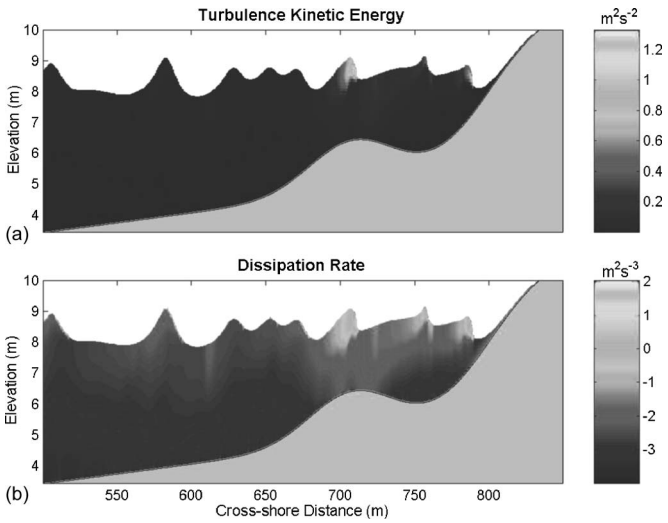

Fig. 5. (a) Snapshot of the model at instance 1,650 s into the run, shaded by TKE. Scale to the right of the panel indicates TKE intensity in $m^2\ s^{-2}$. Wave breaking is determined from the average TKE in the top 10 cm of the water column; (b) snapshot at the same instant, shaded by dissipation rate. Scale to the right of the panel indicates dissipation rate in $m^2\ s^{-3}$, on log 10 scale.

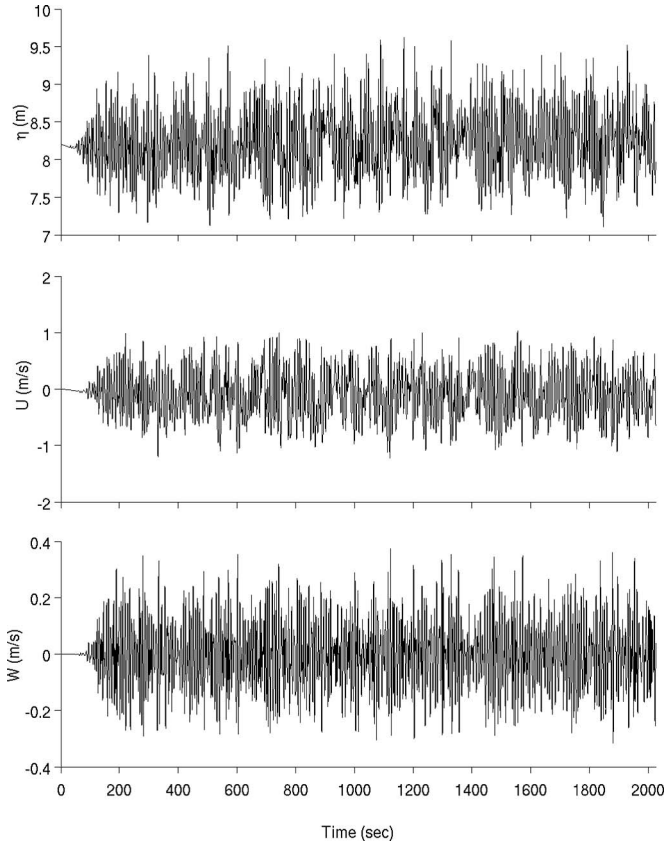

Fig. 6. Time series of η, u, and w from spatial location $x=250$ m in the domain. Initial calm period represents time lag for wave disturbance to reach 250 m from inflow boundary.

breaking is measured optically from land-based video cameras. We use TKE, rather than dissipation, as the model indicator for wave breaking because it is assumed that the field methods detect aeration due to turbulent water motions.

George et al. (1994) measured turbulence intensities below the trough level in the surf zone at Scripps Beach, La Jolla, Calif., using hot film anemometer data. Wave heights ranged from 50 to 120 cm. Our modeled near-surface TKE in breaking waves are about 1.0 $m^2 s^{-2}$. These values normalized by $(gh)^{1/2}$ are approximately 0.2, about an order of magnitude higher than reported by George et al. However, below the trough level, our model TKE levels are of the same order as George et al. Similarly, modeled dissipation estimates are comparable to George et al. below the trough where their field measurements were made.

Fig. 6 shows time series of η, u, and w at a location 250 m from the inflow boundary. There is no visible trend and the constant variance over the run indicates an approximately stationary time series. Low frequency fluctuations are observed in the model time series, but they do not appear to grow in time. The initial calm period results from the time lag for wave disturbances to reach 250 m. Additionally a linear damping filter with 100 s width suppresses transient motions at the start of the run, thus initial wave motions in the time series are small.

Some indication of reflected wave energy was observed (Chopakatla 2003). Re-reflection of these incident waves off the seaward boundary did not appear to adversely affect subsequent results, although it should be pointed out that for steeper beach slopes this problem could limit model performance. Troch and De Rouch (1999) developed methods for reducing the trapping of reflected waves in the domain with active wave absorbing boundary conditions, however their methods were not applied to the present study.

The input wave conditions, taken from field observation, had marked wave groups with periods ranging 50–100 s. The wave groups show strong temporal modulation seaward of the break point, and are largely destroyed by wave breaking inside the surf zone. In nature low frequency (infragravity) waves are generated by nonlinear wave interactions with time and length scales associated with the wave groups. These motions propagate up- and downcoast as edge waves, or are radiated to deep water as seaward propagating (leaky) waves. However, the model is run in a two-dimensional domain, and only allows for shore-normally standing infragravity waves, which are not allowed to escape the domain at the seaward boundary. These model-generated long waves are thus trapped artificially within the domain creating seiches at various frequencies. Simulations run over a linear beach profile and smaller domain size indicate that specific seiching frequencies may resonate depending on the domain characteristics (Chopakatla 2003). These resonant seiches cannot be quantitatively related to the field data, thus our discussion of model performance is limited to incident wave frequencies and mean flows. Model data showed higher infragravity energy than observed (Chopakatla 2003), but the motions did not appear to grow in time (Fig. 6) and did not impact the results adversely.

In order to quantify wave breaking in the model simulation and subsequently compare with field observations, the location of wave crests must be identified and then a determination of whether the crest is breaking or not must be made. Identifying individual wave crests is accomplished in the time domain of each cross-shore location following methods of and Guza (1983). First, the time series of sea surface elevation is filtered to remove both low and high frequency motions using a bandpass filter in the frequency domain such that only wave motions with frequencies in the range 0.05–0.5 Hz are considered. A zero-up crossing method is then used to determine sea surface elevation maxima for each individual wave at each location.

Once the wave crest is identified using the time domain method, the wavelength, crest-trough distance, and maximum slope of the front face of the wave, Θ, were calculated using the space series at each wave crest location. Spatial domain methods are similar to the time domain methods in that filtered, zero-up crossing methods were applied to find trough elevations just shoreward of the wave crests, and distances to the next shoreward crest. Θ is determined between the crest-to-trough excursion. These data are used in conjunction with breaking wave analysis to examine bulk properties of breaking waves.

Once individual wave crests are identified, a method was developed to distinguish those waves that are breaking from those that are not. In general, we assume that wave breaking is characterized by an increase in turbulence at or very near the sea surface. However, the level at which to set a turbulence threshold to identify a breaking wave is not known, primarily owing to the lack of field observational data or theoretical guidance. The procedure adapted here was to average the total amount of turbulent kinetic energy in the upper 10 cm of the water column closest to the sea surface and then find the maximum turbulence kinetic energy, Γ, between the crest and trough. As the turbulence level can be effected by nonlocally generated turbulence advected and diffused laterally and vertically, we do not know a priori what the turbulence threshold level should be, or if it is spatially or temporally varying.

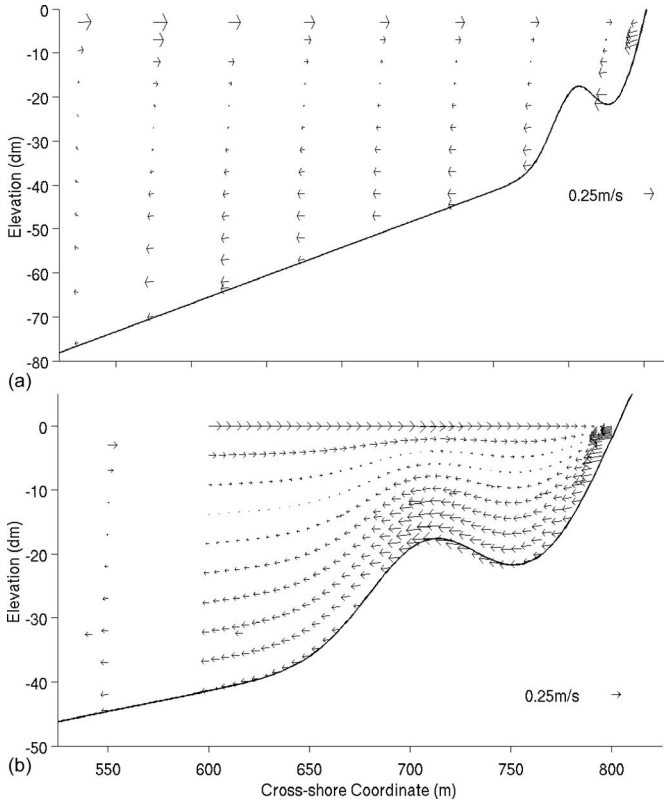

Fig. 7. (a) Mean velocity vectors for selected locations in the large scale array; (b) all locations in the dense array in and around the surf zone. Velocities are averaged from 200 to 2025 s and scaled by a vector of magnitude 0.25 m/s in horizontal direction (shown in the lower right-hand corner).

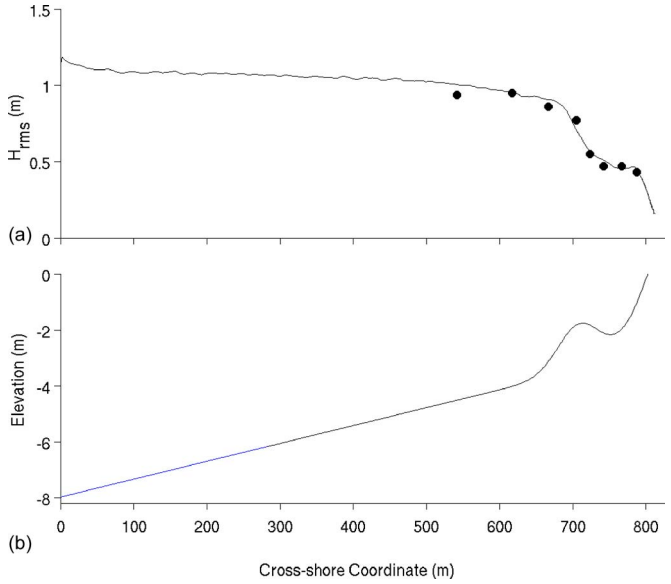

Fig. 8. Model results evaluated over a 35.5 min run time, excluding 200 s spin-up period: (a) RMS wave heights; (b) bathymetry. H_{RMS} observations from the field are shown by closed circles.

In field experiments, wave breaking is most commonly associated with the entrapment of air bubbles at or near the sea surface. The bubbles (and foam) produce a visual contrast in the intensity that can be captured photographically. Quantification of wave breaking during the Delilah field experiment was accomplished with video image processing methods (Lippmann and Holman 1991) without the use of in situ turbulence data to compare with. Thus, for model–data comparisons needed to verify the FLOW-3D model, a turbulence threshold must be determined that makes the breaking distributions consistent with the field observations. In doing so, a range of turbulence thresholds were used to determine the presence of a breaking wave and the threshold that best represents the data chosen (discussed later).

Model mean flow calculated over the 35.5 min record is shown as vectors in Fig. 7. As expected the flow pattern shows a strong vertical variation, with onshore flow near the sea surface and a seaward return flow down in the water column. This pattern is qualitatively similar to mean flow measured at various field experiments (e.g., Haines and Sallenger 1994; Garcez Faria et al. 2000). Of particular interest is the strong undertow increasing over the shallows of the sand bar. This flow pattern decreases seaward, as expected. To conserve momentum, a circulation must be set up in the domain. The mean vertical flow (hence the circulation) is weak, although right at the seaward boundary the vertical velocities increase slightly. In smaller scale tests over planar bathymetry, a very strong circulation developed close to the seaward boundary after a short time of about 30 wave periods (Chopakatla 2003), a result also noted by Bradford (2000). By increasing the domain size to the prototype scale, this strong circulation is diminished, and does not appear to effect results obtained in our field scale model discussed here.

Model–Field Data Comparisons

To verify the modeled wave transformations, H_{RMS} was computed every meter across the domain for the 35.5 min run and compared with field observations. The results (Fig. 8) are quite good with RMS error of about 0.041 m, about the same as obtained with previous wave transformation models (e.g., Fig. 1; and Guza 1983; Lippmann et al. 1996a) but without the need to specify wave breaking parameters or criteria a priori. Note that the modeled wave height transformation does not depend on the threshold levels discussed earlier, as those are used only to determine the fraction of waves breaking (discussed later).

The model–data comparison of mean flow obtained at the location of the in situ sensors is shown in Fig. 9. The modeled flow is qualitatively similar to the observations, with stronger undertow over the shallows of the sandbar and decreasing flow seaward of the surf zone. The model overpredicts the mean undertow onshore and seaward of the bar, and underpredicts the maximum undertow over the bar. In general, the model does a reasonable job of reproducing the flow field despite the obvious limitations imposed by the two-dimensional domain.

In order to verify wave breaking distributions, Q_b were calculated for a number of turbulence thresholds and compared them with observations obtained in the field with video techniques. A threshold value of 0.5 $\mathrm{m^2\,s^{-2}}$ gives the best comparison with the field data, well capturing the increase across the sandbar and diminished, but substantial breaking through the bar-trough region (Fig. 10). The modeled breaking distribution compares well with the observed values from seaward of the sandbar through the surf zone, suggesting that the methods for detecting breakers in the model are similar in character to the optical methods used in the field. Breaking data were not collected in the field right near

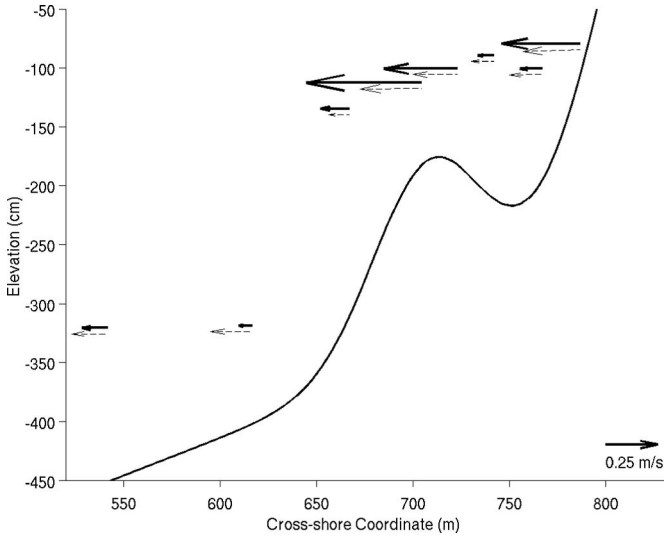

Fig. 9. Comparison of model (thin dashed vectors) and field (thick solid vectors) mean velocities at locations where the field data were collected. Model vectors are offset by 5 cm vertically for clarity. Model vectors include horizontal and vertical velocities. Velocities are averaged over 35.5 min. Scale vector of magnitude 0.25 m/s is shown in the lower right-hand corner.

the shoreline, thus the model results close to shore cannot be verified. Right near the shoreline it would be expected that nearly all waves would be breaking. However, owing to low frequency (infragravity) oscillations, the distribution of total waves varies depending on the height of the run-up. Thus, the fraction of wave breaking tends to zero as the run-up reaches its maximum extent.

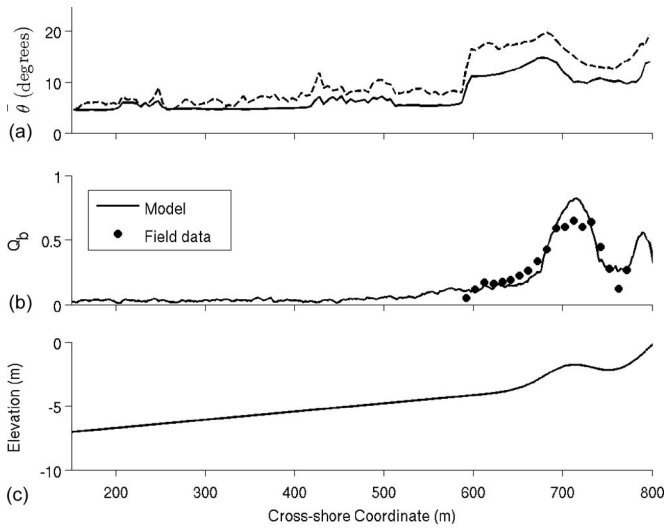

Fig. 10. (a) Average instantaneous wave slope between the crest and trough for both breaking (dashed line) and nonbreaking waves (solid line), spatially averaged every 5 m and temporally averaged over postspin off period (200–2025 s); (b) breaking fraction averaged over every 2 m spatially (TKE threshold=0.5 $m^2 s^{-2}$) and also shows the field observations as closed circles; and (c) bathymetry for reference

Discussion

In previous models, wave transformation across the surf zone was determined by specifying the wave breaking distribution or criteria ahead of time. These distributions and criteria have been based largely on observation from the field, and in general have performed very well in determining the wave height transformation for both barred and nonbarred bathymetric profiles (e.g., and Guza 1983; Lippmann et al. 1996a). However, corresponding calculations of the spatial distribution of mean alongshore currents on barred beach profiles have not been well reproduced when using stress calculations derived from the wave models (Church and 1993; Lippmann et al. 1996b). Consequently, numerous approaches have been attempted to improve the spatial distribution of the wave stress, particularly in the trough of the sandbar where longshore currents are often maximum (Thornton and Kim 1993).

One limitation of the early transformation models is that breaking criteria must be specified at the start of the run. Although this works well for wave height prediction, it does not lead to good representation of the observed spatial wave breaking patterns (e.g., Fig. 1). The inclusion of wave rollers in the time and depth-averaged longshore momentum balance can lead to improved fit to the spatial distribution of observed breaking pattern, but requires iterative fit of two free parameters (Lippmann et al. 1996b).

In CFD models, wave breaking occurs as a consequence of the fluid dynamics, and does not require a priori specification of any free parameters (all turbulence parameters are obtained from the literature as accepted values based on theoretical or laboratory observation). The model simulations are able to well reproduce the observed wave height transformation (Fig. 8), the mean undertow (Fig. 9), and wave breaking distributions (Fig. 10). This suggests that CFD models can be used to create a numerical laboratory at prototype field scales to study in detail the wave transformation and breaking process.

One limitation of the CFD approach is that the turbulence threshold level was chosen to give the best fit to the observations. In effect, what the model–data comparisons show is that the video observations in the field identify the wave breakers which produce a given amount of turbulence at breaking. The actual value of the chosen breaking threshold could, in fact, be different. This limitation of the CFD models only arises when verification to a separate breaking observation is made; for example, with video data. A better test would be to compare field observations of turbulence kinetic energy or dissipation directly with the model. This work is being pursued as part of ongoing research.

The identification of individual wave crests, breaking wave crests, crest-trough distance, and wavelengths allows for an approximation of the spatial variation of breaking criteria commonly used in other models. Of particular interest is the spatial variation of the maximum slope on the front face of the wave, Θ, calculated by finding the maximum surface slope between crest and trough. Fig. 10 shows the variation of average surface slope, $\bar{\Theta}$, as a function of cross-shore distance. This parameter is a good general indicator of shape of the wave. In deep water, surface slopes are around 5° for both breaking and nonbreaking waves indicating a very gradually sloping wave. However, wave slopes increase rapidly past 600 m and close to the sandbar, and at location just seaward of maximum breaking, $\bar{\Theta}$ attains a maximum value close to 20°. Inside the bar crest, breaking slopes gradually relax to a value of around 12°.

Criteria for wave breaking in time-domain Boussinesq models are often determined by the maximum slope on the front face of the wave, Θ (Deigaard 1989; Schaffer et al. 1993). Schaffer et al. used Θ values of 20° as breaking criteria. In their model, any wave with a slope above this value is breaking. Our modeled Θ (Fig. 10) show similar breaking slopes, suggesting that the criteria used in Boussinesq models is appropriate. Further, Schaffer et al. (1993) have reformed waves taking on a terminal slope of 10°, similar to our model values for nonbreaking waves in the surf zone.

Conclusions

In this work, we have adapted the commercial CFD model FLOW-3D to simulate two-dimensional wave transformation and wave breaking across a naturally barred beach profile. The model is driven by observations of near-bottom wave pressure at the seaward boundary, and can simulate pressures, velocities, turbulent kinetic energy, and dissipation at each grid point across the beach profile up to the swash. The model domain spans approximately 800 m across shore from 8 m water depth to the foreshore where wave motions are allowed to run up and down the beach face. Uniform grid cells in the domain are 0.5 m horizontally and 0.1 m vertically.

Wave breaking is a natural consequence of the fluid dynamics and does not require the use of empirical formulations for breaking criteria or probability density functions. Wave dissipation is determined by a coupled turbulence closure scheme based on the turbulent kinetic energy and dissipation transport equations with the RNG extension developed by Yakhot et al. (1992).

The model is run over an analytical form (Lippmann et al. 1999) for the measured bathymetry obtained during the 1990 Delilah Field Experiment (Birkemeier 1991). The model simulations are verified with observations of pressure and velocity obtained in the field at eight locations spanning the surf zone (Thornton and Kim 1993), as well as video-based observations of wave breaking distributions (Lippmann and Holman 1991). Although the model is limited to two-dimensional wave propagation without consideration of nonnormal angle of incidence or alongshore flow, the model is able to well simulate bulk properties of the wave transformation, mean cross-shore flow, and wave breaking distributions. Of particular interest is the spatial distribution of the wave breaking pattern, which is not reproduced with existing ensemble-averaged wave transformation models (e.g., Thornton and Guza 1983; Lippmann et al. 1996a). The results suggest that FLOW-3D can thus be used as a numerical laboratory for detailed studies of the nonlinear wave breaking process.

Acknowledgments

This work was funded by the NOAA Sea Grant Technology program. This work was completed while S. C. C. was at Ohio State University, and J. E. R. was employed by Earth Tech., Inc., and Alden Research Lab, Inc. The writers thank J. Brethour and D. Souders of Flow Science, Inc., for assistance with development of boundary conditions, data extraction modules, and operation of the model and D. Foster, H. Smith, and K. Bedford for helpful comments and suggestions. Observations of surf zone pressures and velocities were collected by E. Thornton and T. Stanton of the Naval Postgraduate school, the video data were collected by R. Holman of Oregon State University, and the pressure data in 8 m water depth were collected by the staff of the U.S. Army Field Research Facility. The writers gratefully acknowledge the use of their data in this work.

Notation

The following symbols are used in this paper:

a_1, a_2 = synthetic beach profile fitting constants;
C_μ = empirical turbulence constant;
C_1, C_2 = empirical turbulence constants;
D_k = diffusion term;
D_ε = dissipation term;
d = normal distance from wall to computed velocity;
F = fluid fraction;
f = wave frequency;
g = acceleration due to gravity;
H = wave height;
H_{RMS} = root-mean-square wave height;
h = water depth;
i, j, l = cell indices in x-, y-, z-directions;
k = turbulence kinetic energy;
L = wavelength;
n = incremental time level;
P = shear production term;
p = fluid pressure;
Q_b = fraction of wave field that is breaking;
S_r = fluid volume sink rate;
T_x, T_z = terms representing spatial gradients in cross-shore direction;
t = time;
$\tilde{u}$ = component of u parallel to wall orientation;
u, w = horizontal and vertical water-particle velocity;
$u*$ = local shear velocity;
V_i, V_f = fluid volume in domain at start and end of run;
x = cross-shore coordinate;
x_c = cross-shore location of bar crest;
y = alongshore (up/downcoast) coordinate;
z = vertical coordinate;
α = advection weighting term;
β = RNG turbulence model variable;
β_1 = empirical foreshore profile slope;
β_2 = empirical offshore profile slope;
Γ = maximum turbulence kinetic energy;
Δt = time step;
Δx = horizontal grid size;
Δz = vertical grid size;
δp = fluid pressure correction term;
ε = dissipation rate of k;
η = water surface elevation;
Θ = maximum slope of front face of wave;
$\bar{\Theta}$ = temporal average slope of front face of wave;
ν = kinematic eddy viscosity of water;
ν_T = eddy viscosity;
ρ = density of water;
σ_k = empirical turbulence diffusion constant;
σ_ε = empirical dissipation constant;
τ = shear stress; and
Ω = overrelaxation turbulence constant.

References

Battjes, J. A., and Jannsen, J. P. F. M. (1978). "Energy loss and set-up due to breaking of random waves." *Proc., 16th Int. Conf. on Coastal Engineering*, ASCE, New York, 569–587.

Birkemeier, W. A. (1991). "Delilah near processes experiment: Data summary." *Miscellaneous Rep.*, Coastal Engineering Research Center, Field Research Facility, U.S. Army Eng. Waterw. Exp. Sta., Vicksburg, Miss.

Bradford, S. F. (2000). "Numerical simulation of surf zone dynamics." *J. Waterway, Port, Coastal, Ocean Eng.*, 126(1), 1–13.

Chen, Y., Guza, R. T., and Elgar, S. (1997). "Modeling spectra of breaking surface waves in shallow water." *J. Geophys. Res.*, 102, 25035–25046.

Chopakatla, S. C. (2003). "A CFD model for wave transformation and breaking in the surf zone." MS thesis, The Ohio State Univ., Columbus, Ohio.

Church, J. C., and Thornton, E. B. (1993). "Effects of breaking wave induced turbulence within a longshore current model." *Coastal Eng.*, 20, 1–28.

Deigaard, R. (1989). "Mathematical modeling of waves in the surf zone." *Progress Rep. No. 69*, ISVA Technical Univ. of Denmark, Lyngby, Denmark, 47–59.

Flow Science Inc. (2002). *FLOW-3D user's manual*, Los Alamos, N.M.

Garcez Faria, A. F., Thornton, E. B., Lippmann, T. C., and Stanton, T. P. (2000). "Undertow over a barred beach." *J. Geophys. Res.*, 105(C7), 16999–17010.

George, R., Flick, R. E., and Guza, R. T. (1994). "Observations of turbulence in the surf zone." *J. Geophys. Res.*, 99, 801–810.

Guza, R. T., and Thornton, E. B. (1980). "Local and shoaled comparisons of sea surface elevations, pressure and velocities." *J. Geophys. Res.*, 85, 1524–1530.

Haines, J. W., and Sallenger, A. H. (1994). "Vertical structure of mean cross-shore currents across a barred surf zone." *J. Geophys. Res.*, 99(C7), 14223–14242.

Harlow, F. H., and Welch, J. E. (1965). "Numerical calculation of time-dependent viscous incompressible flow of fluid with free surface." *Phys. Fluids*, 8, 2182–2189.

Hirt, C. W., and Nichols, B. D. (1981). "Volume of fluid (VOF) method for the dynamics of free boundaries." *J. Comput. Phys.*, 39, 201–225.

Kaihatu, J. M., and Kirby, J. T. (1995). "Nonlinear transformation of waves in finite water depth." *Phys. Fluids*, 7(8), 1903–1914.

Kennedy, A. B., Chen, Q., Kirby, J. T., and Dalrymple, R. A. (2000). "Boussinesq modeling of wave transformation, breaking and runup. I: 1D." *J. Waterway, Port, Coastal, Ocean Eng.*, 126(1), 39–47.

Lin, P., and Liu, P. L. F. (1998). "A numerical study of breaking waves in the surf zone." *J. Fluid Mech.*, 359, 239–264.

Lippmann, T. C., Brookins, A. H., and Thornton, E. B. (1996a). "Wave energy transformation on natural profiles." *Coastal Eng.*, 27, 1–20.

Lippmann, T. C., Herbers, T. H. C., and Thornton, E. B. (1999). "Gravity and shear wave contributions to nearshore infragravity motions." *J. Phys. Oceanogr.*, 29, 231–239.

Lippmann, T. C., and Holman, R. A. (1991). "Phase speed and angle of breaking waves measured with video techniques." *Proc., Conf. Coastal Sediments '91*, ASCE, New York, 542–556.

Lippmann, T. C., Thornton, E. B., and Reniers, A. J. H. (1996b). "Wave stress and longshore current on barred profiles." *Proc., Conf. Coastal Dynamics '95*, ASCE, Reston, Va., 401–412.

Schaffer, H. A., Madsen, P. A., and Deigaard, R. (1993). "A Boussinesq model for waves breaking in shallow water." *Coastal Eng.*, 20, 185–202.

Thornton, E. B., and Guza, R. T. (1983). "Transformation of wave height distribution." *J. Geophys. Res.*, 88, 5925–5938.

Thornton, E. B., and Kim, C. S. (1993). "Longshore current and wave height modulation at tidal frequency inside the surf zone." *J. Geophys. Res.*, 98(C9), 16509–16519.

Ting, F. C. K., and Kirby, J. T. (1995). "Dynamics of surf-zone turbulence in a strong plunging breaker." *Coastal Eng.*, 24, 177–204.

Ting, F. C. K., and Kirby, J. T. (1996). "Dynamics of surf-zone turbulence in a spilling breaker." *Coastal Eng.*, 27, 131–160.

Troch, P., and De Rouch, J. (1999). "An active wave generating-absorbing boundary condition for VOF type numerical model." *Coastal Eng.*, 38, 223–247.

Yakhot, V., Orszag, S. A., Thangam, S., Gatski, T. B., and Speziale, C. G. (1992). "Development of turbulence models for shear flows by a double expansion technique." *Phys. of Fluids*, 4, 1510–1520.